# Semiclassical approximations to diffractive effects in the annulus billiard

N. C. Snaith* and D. A. Goodings
*Department of Physics and Astronomy, McMaster University, Hamilton, Ontario, Canada L8S 4M1*
(Received 27 August 1996; revised manuscript received 18 December 1996)

The semiclassical theory formulated by Bogomolny [E. B. Bogomolny, Nonlinearity **5**, 805 (1992)] employs a transfer operator constructed from classical trajectories that connect points on a suitably chosen Poincaré surface of section. In this paper we study the two-dimensional annulus billiard, and modify Bogomolny's transfer operator to include diffractive paths. The penumbra contributions [H. Primack *et al.*, Phys. Rev. Lett. **76**, 1615 (1996)], which correspond to diffractive paths passing close to the inner circle of the annulus, are found to account for most of the difference between the exact transfer operator and Bogomolny's semiclassical transfer operator. When these diffractive effects are included, the semiclassical energy eigenvalues are brought much closer to the exact quantum energy eigenvalues. [S1063-651X(97)07005-0]

PACS number(s): 05.45.+b, 03.65.Sq

## I. INTRODUCTION

Semiclassical approximations to quantum mechanics often provide insights into the behavior of physical systems that are not obtained by simply solving the Schrödinger equation with appropriate boundary conditions. For nonintegrable systems the Gutzwiller trace formula [1,2] and the closely related dynamical $\zeta$ function [3,4] give a semiclassical description based on the periodic orbits of the classical system. Knowing the classical action, the Maslov index, and the stability index of the shortest periodic orbits of a given system, one can use systematic expansions of the dynamical $\zeta$ function [5–7] to obtain a good approximation to the energy eigenvalues of the quantum system. A comparison of several methods employing periodic orbit theory has been given for the wedge billiard for angles corresponding to hard chaos [8].

The trace formula and the dynamical $\zeta$ function may be regarded as the leading approximation of an expansion in powers of Planck's constant [9–11]. It would appear that it is very difficult to calculate exactly the correction terms corresponding to the next power of $\hbar$ in the expansion. However, there are many systems in which an important correction to standard periodic orbit theory—not necessarily of higher order in $\hbar$—can be obtained by treating diffractive effects in the spirit of the *geometric theory of diffraction* [12,13]. Wirzba and co-workers [14–17] extended periodic orbit theory to include periodic orbits containing *diffractive paths*, i.e., segments in which the wave nature of the particle is of prime importance. They successfully applied their approach to calculating the scattering resonances of two-disk and three-disk systems in two dimensions.

The diffractive paths may have various forms. In one kind the particle wave creeps along a smooth arc of a curved surface, radiating at each point along the creeping path [14–17]. In another, it propagates to and from a vertex—a point on the boundary of the system at which the direction of the tangent changes discontinuously. Examples of this type are paths passing through the vertex of a triangle [18], the vertex of a hyperbola in the limit that it has narrowed down to a straight line [19], either of the vertices of two wedges whose bisectors lie on a common axis [20], and the vertex of the cardioid billiard [21]. Diffractive effects also occur when the system encloses a point scatterer [22], small circular disks [23], or a singular magnetic flux line [24–26]. Still another diffractive effect—the one treated in this paper—occurs under grazing conditions in which some classical trajectories are reflected from a smooth surface while close parallel ones are not. In a recent study of the Sinai billiard, Primack *et al.* [27] derived important diffractive corrections to the semiclassical density of states (and its Fourier transform) by modifying the propagator for paths in the vicinity of the tangent to the circular disk. With the exception of Ref. [22], all of these studies have been carried out in the framework of periodic orbit theory.

A different semiclassical theory, not depending on the periodic orbits of the system, has been developed by Bogomolny [28,29]. The theory is formulated in terms of a transfer operator and a suitably defined Poincaré surface of section (PSS) in configuration space. For a system with two freedoms, the PSS is simply a one-dimensional curve, usually taken to be the boundary in billiard systems. For two freedoms the transfer operator has the form

$$T(q'',q';E)=\sum_{\text{cl.tr.}}\frac{1}{(2\pi i\hbar)^{1/2}}\left|\frac{\partial^2 S(q'',q';E)}{\partial q''\partial q'}\right|^{1/2}\times\exp[iS(q'',q';E)/\hbar-i\nu\pi/2], \qquad (1)$$

where $q'$ and $q''$ are points located on the PSS. The summation is over all classical trajectories which cross the PSS only once in going from $q'$ to $q''$ and have the normal component of the momentum in the same direction at $q'$ and $q''$. For each such trajectory one needs the action at energy $E$, denoted by $S(q'',q';E)$, and the phase index $\nu$, which is related to the number of points on the trajectory at which the semiclassical approximation is not valid.

A finite approximation to the transfer operator in coordinate space can be constructed by dividing the accessible part of the PSS into $N$ cells, the $n$th cell centered on $q_n$ having

*Present address: School of Mathematics, University of Bristol, Bristol BS8 1TW, England.

 

width $\Delta_n$. In terms of the transfer operator $T(q_m,q_n;E)$ from $q_m$ in cell $m$ to $q_n$ in cell $n$, the matrix element $T_{mn}(E)$ is defined to be

$$T_{mn}(E)=T(q_m,q_n;E)(\Delta_m\Delta_n)^{1/2}. \tag{2}$$

Then the condition for an energy eigenvalue is that

$$\det[\,\delta_{mn}-T_{mn}(E)]=0. \tag{3}$$

We note that this equation will be satisfied whenever one of the eigenvalues of the $T$ matrix is equal to unity. Bogomolny's theory offers an appealing alternative to periodic orbit theory, for both integrable and nonintegrable systems [30,31]. Its main advantage is that, instead of having to find systematically the periodic orbits of a given system and calculate their properties, one has to calculate only the action, its second derivative, and the phase index for classical trajectories connecting points on the PSS. Furthermore, it has been found that the resulting semiclassical energy eigenvalues converge to definite values as the cell size in *phase space* (constructed using the coordinate on the PSS together with its conjugate momentum) approaches roughly $h/10$ [30].

The question we set out to investigate is how to modify Bogomolny's theory to include diffractive paths, such as occur in the geometric theory of diffraction [12,13], in addition to the purely classical trajectories required by Eq. (1). In this paper we shall describe how this can be done for a simple system, the annulus billiard. If the outer circle of the annulus is chosen to be the Poincaré surface of section in configuration space, one might expect that diffraction will be important for paths that pass close to the inner circle of the annulus. As mentioned above, such paths have been shown by Primack *et al.* [27] to be very important for the Sinai billiard, which differs from the annulus billiard only in having a square outer boundary instead of a circular one.

An attractive feature of the annulus billiard is the fact that the circular symmetry makes it possible to obtain the energy eigenvalues of the system by a simple procedure. This enables us to calculate the energy eigenvalues using different semiclassical approximations. We are particularly interested in seeing how the results calculated from Bogomolny's transfer operator constructed from purely classical trajectories compare with the results obtained with the inclusion of diffractive paths.

In Sec. II we describe the exact Green function for the quantum system, and show how to construct the corresponding transfer operator and its eigenvalue curves (as a function of the energy). Section III describes semiclassical approximations to the exact Green function in three different regions—the illuminated region, the penumbra, and the shadow region. In Sec. IV, the semiclassical transfer operator, modified to include diffractive paths, is shown in the three different regions and compared with the exact quantum-mechanical transfer operator. The corresponding semiclassical energy eigenvalues, with and without diffractive corrections, are calculated and compared with the exact energies in Sec. V. As a standard for comparison, we also give the energy eigenvalues calculated by the simple Einstein-Brillouin-Keller (EBK) quantization procedure. Our main findings are summarized in Sec. VI.

## II. EXACT GREEN FUNCTION AND TRANSFER OPERATOR FOR THE ANNULUS BILLIARD

The annulus billiard consists of a particle confined to the region between two concentric circles of radii $a$ and $R$, with $a<R$. Since the potential is zero in the annular region, the Green function for the quantum system satisfies the equation

$$-\frac{\hbar^2}{2m}\nabla_{\mathbf{r}}^2G(\mathbf{r},\mathbf{r}';k)-\frac{\hbar^2k^2}{2m}G(\mathbf{r},\mathbf{r}';k)=-\delta(\mathbf{r}-\mathbf{r}'). \tag{4}$$

The energy $E$ of the particle has been written as $\hbar^2k^2/(2m)$, where $\hbar k$ is the magnitude of the linear momentum and $m$ is the mass of the particle. Representing $\mathbf{r}$ by $(r,\theta)$ and $\mathbf{r}'$ by $(r',\theta')$, one can show that the solution of Eq. (4) which is zero on the circle of radius $a$ and has the form of an outgoing wave in the annular region is [23,27]

$$G(\mathbf{r},\mathbf{r}';k)=\sum_{l=-\infty}^{\infty}g_l(r,r';k)\exp[il(\theta'-\theta)], \tag{5}$$

$$g_l(r,r';k)=-\frac{im}{4\hbar^2}[H_l^-(kr_<)+S_l(ka)H_l^+(kr_<)]H_l^+(kr_>), \tag{6}$$

where $r_<$ is the lesser and $r_>$ the greater of $r$ and $r'$, and $S_l(ka)=-H_l^-(ka)/H_l^+(ka)$. $H_l^-(x)$ and $H_l^+(x)$ are the Hankel functions defined in terms of the ordinary Bessel functions as $H_l^{\pm}(x)=J_l(x)\pm iY_l(x)$.

We now apply the boundary integral method [32–34] to the outer circle of radius $R$, regarded as the boundary $B$. Imposing the condition that the wave function $\psi(\mathbf{r})$ is zero on $B$, one finds that when $\mathbf{r}$ and $\mathbf{r}'$ lie on the boundary,

$$\oint_B G(\mathbf{r},\mathbf{r}';k)\frac{\partial\psi(\mathbf{r}')}{\partial n_{\mathbf{r}'}}dl'=0, \tag{7}$$

where $\partial\psi(\mathbf{r}')/\partial n_{\mathbf{r}'}$ is the normal derivative at $\mathbf{r}'$, and $dl'$ is an infinitesimal increment along the boundary. This is the condition that must be satisfied when $k$ corresponds to an energy eigenvalue of the Schrödinger equation for the particle.

Equation (7) can be solved by dividing the boundary $B$ into $N$ cells of width $\Delta=2\pi R/N$, with centers at positions $\mathbf{r}_i=(R,\theta_i)$, $i=0,1,\ldots,N-1$ $(\mathbf{r}_N=\mathbf{r}_0)$. Denoting $[\partial\psi(\mathbf{r}')/\partial n_{\mathbf{r}'}]\Delta$ at position $\mathbf{r}_j$ by $A_j$, we obtain

$$\sum_{j=0}^{N-1}G(\theta_i,\theta_j;k)A_j=0,\quad i=0,1,\ldots,N-1. \tag{8}$$

A nontrivial solution exists when

$$\det[G(\theta_i,\theta_j;k)]=0. \tag{9}$$

However, this equation cannot be used as it stands because the diagonal elements (for which $\mathbf{r}=\mathbf{r}'$) are infinite.

Because of the circular symmetry of the annulus, we need only consider the $N$ distinct elements $G(\theta_0,\theta_j;k)$ with $\theta_j=j(2\pi/N)$. Despite the singularity at $j=0$, it is instructive to calculate $|G(\theta_0,\theta_j;k)|$ as a function of the angle $\theta_j-\theta_0$. This is accomplished by setting $\theta'-\theta=\theta_j-\theta_0$, and

$r=r'=R$ in Eqs. (5) and (6). For simplicity we shall henceforth denote $\theta_j-\theta_0$ by $\theta$ and the corresponding Green function by $G(\theta;k)$. Calculations of $|G(\theta;k)|$ as a function of $\theta$ for two different values of $k$ are shown as the solid curves in Figs. 4–6. (The values of $k$ were chosen to be $k$ eigenvalues close to 10 and 50, in each case. However, there is no visible change in any of the plotted curves in the figures if $k$ is taken to be exactly 10 or 50, i.e., not corresponding to a $k$ eigenvalue.) We shall refer to these curves as the exact Green function since they were calculated from the exact solution of Eq. (4) given by Eqs. (5) and (6). Note that since $|G(-\theta;k)|=|G(\theta;k)|$, we have plotted $|G(\theta;k)|$ only for $\theta$ in the range between 0 and $\pi$.

The problem of the singular elements $G(\theta_0,\theta_0;k)$ in Eq. (9) can be dealt with by the following procedure [28], which leads to Bogomolny's transfer operator. First we construct the matrix representation of the Green function $G(\theta,\theta';k)$ for $\mathbf{r}=(R,\theta)$ and $\mathbf{r}'=(R,\theta')$ in the set of orthonormal basis functions $\{\exp(il\theta)/\sqrt{2\pi}\}$:

$$G_{ll'}(k)=\frac{1}{2\pi}\int_0^{2\pi}d\theta\int_0^{2\pi}d\theta'\exp(il\theta)G(\theta,\theta';k)\times\exp(-il'\theta'). \tag{10}$$

From the correct form for $G(\theta,\theta';k)$ when $\theta'$ is very close to $\theta$ [35,28], one can show that, when $|\theta-\theta'|\ll 1$,

$$G_{ll'}(k)=-\frac{im}{\hbar^2}\frac{1}{(k^2R^2-l^2)^{1/2}}\delta_{ll'}, \tag{11}$$

which is singular when $|l|=kR$. [If, for the moment, we think of $l$ as a continuous variable representing the classical angular momentum (in units of $\hbar$), it is easy to see that the maximum value of $|l|$ is $kR$.] Following Bogomolny [28], we now modify the condition $\det[G_{ll'}(k)]=0$ for a $k$ eigenvalue to

$$\det[\widetilde{G}_{ll'}(k)]=0,\quad \widetilde{G}_{ll'}(k)=c_l c_{l'}G_{ll'}(k), \tag{12}$$

where the constants $c_l$ and $c_{l'}$ are given by

$$c_l=\frac{\hbar}{\sqrt{-im}}(k^2R^2-l^2)^{1/4}. \tag{13}$$

Substituting Eqs. (5) and (6) in Eq. (10), one finds that the matrix $\widetilde{G}_{ll'}(k)$ is diagonal:

$$\widetilde{G}_{ll'}(k)=\frac{2\pi i\hbar^2}{m}(k^2R^2-l^2)^{1/2}g_l(R,R;k)\delta_{ll'},\quad |l|\leqslant kR. \tag{14}$$

From Eq. (12), a $k$ eigenvalue occurs whenever *any* of these diagonal elements is equal to zero. Thus, from Eq. (6), a $k$ eigenvalue of the Schrödinger equation occurs when

$$H_l^+(kR)H_l^-(ka)-H_l^+(ka)H_l^-(kR)=0, \tag{15}$$

or when

$$J_l(ka)Y_l(kR)-Y_l(ka)J_l(kR)=0. \tag{16}$$

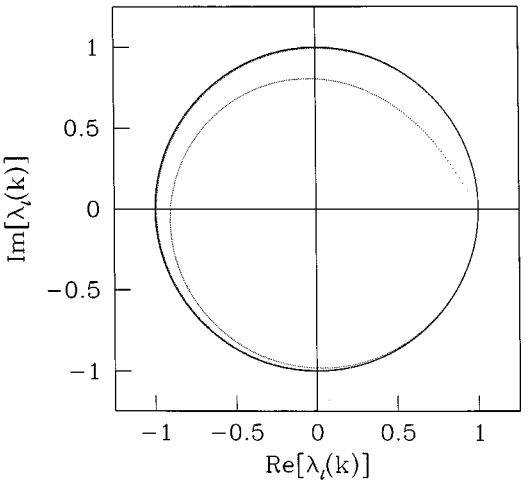


FIG. 1. A typical plot of $\lambda_l(k)$ in the complex plane.

By solving the Schrödinger equation for the annulus with Dirichlet boundary conditions on both circles, one can show that Eq. (16) is the condition for an exact energy eigenvalue. For each value of $l$ there is an infinite number of distinct $k$ values satisfying Eq. (15) or (16). (We shall refer to *energy eigenvalues* and *k eigenvalues* interchangeably in what follows.)

Condition (12) for a $k$ eigenvalue may also be written as

$$\det[\delta_{ll'}-T_{ll'}(k)]=0,\quad T_{ll'}(k)=-\widetilde{G}_{ll'}(k)+\delta_{ll'}, \tag{17}$$

where the matrix $T_{ll'}(k)$ is the quantum-mechanical version of Bogomolny's transfer operator [28] in the $l$ representation. Since the $T$ operator is diagonal in this representation, its eigenvalues as a function of $k$ are, from Eqs. (14) and (17),

$$\lambda_l(k)=-\frac{2\pi i\hbar^2}{m}(k^2R^2-l^2)^{1/2}g_l(R,R;k)+1$$
$$=\frac{\pi}{2}(k^2R^2-l^2)^{1/2}[H_l^+(kR)H_l^-(ka)-H_l^+(ka)H_l^-(kR)]\frac{H_l^+(kR)}{H_l^+(ka)}+1, \tag{18}$$

for $l=0,\pm1,\pm2,\ldots$. An energy eigenvalue of the Schrödinger equation occurs whenever $\lambda_l(k)=1$. (Clearly, $\lambda_{-l}(k)=\lambda_l(k)$, implying that the eigenvalue curves are doubly degenerate, except when $l=0$.) A typical plot of $\lambda_l(k)$ in the complex plane is shown in Fig. 1. The curve starts out at $+1$ when $k=l/R$, and, after an ''initial transient,'' moves onto the unit circle. As $k$ continues to increase, it winds around the unit circle in a counterclockwise direction, yielding a $k$-eigenvalue each time it crosses the real axis at $+1$. Similar plots of $T$-matrix eigenvalue curves have been given previously by Haggerty [31], Lefebvre [36], and Rouvinez and Smilansky [37].

For comparison with the semiclassical approximations to the transfer operator to be described later in the paper, we require matrix elements of $T$ in the $\theta$ representation. As before, the PSS (the outer circle) is divided into $N$ cells of

width $\Delta\theta=2\pi/N$, with centers at positions $\mathbf{r}_i=(R,\theta_i)$, $i=0,1,\ldots,N-1$. In the $\theta$ representation, the matrix element connecting cells $i$ and $j$ is

$$T(\theta_j,\theta_i;k)=\frac{1}{2\pi}\sum_{l=-\infty}^{\infty}\sum_{l'=-\infty}^{\infty}\exp(il'\theta_i)T_{ll'}(k)\times\exp(-il\theta_j)\Delta\theta. \tag{19}$$

Because of the circular symmetry, there are only $N$ distinct matrix elements $T_j(k)=T(\theta_j,0;k)$, obtained by putting $\theta_i=0$, $\theta_j=j(2\pi/N)$. Since $T_{ll'}(k)$ is diagonal, from Eqs. (14), (17), and (19), we find

$$T_j(k)=\frac{1}{2\pi}\sum_{l=-kR}^{kR}\left[-\frac{2\pi i\hbar^2}{m}(k^2R^2-l^2)^{1/2}g_l(R,R;k)+1\right]\times\exp(-il\theta_j)\Delta\theta. \tag{20}$$

Note that the sum over $l$ has been restricted to integers in the range between $-kR$ and $kR$ in order that $k^2R^2-l^2$ be positive. From Eqs. (2) and (20), we can deduce the exact transfer operator in the form of Eq. (1):

$$T_{exact}(\theta;k)=\frac{1}{2\pi}\sum_{l=-kR}^{kR}\left[-\frac{2\pi i\hbar^2}{m}(k^2R^2-l^2)^{1/2}\times g_l(R,R;k)+1\right]\exp(-il\theta), \tag{21}$$

where $\theta=|\theta''-\theta'|$.

The transfer matrix $T(\theta_j,\theta_i;k)$ has the circulant form

$$\begin{pmatrix} T_0 & T_1\cdots & T_{N-2} & T_{N-1}\\ T_{N-1} & T_0\cdots & T_{N-3} & T_{N-2}\\ \vdots & \vdots\ddots & \vdots & \vdots\\ T_2 & T_3\cdots & T_0 & T_1\\ T_1 & T_2\cdots & T_{N-1} & T_0 \end{pmatrix}, \tag{22}$$

in which the matrix elements $T_j$ are given by Eq. (20). Following Lefebvre [36], we make use of the fact that the eigenvalues of such a matrix can be expressed in the simple form

$$\lambda_n(k)=\sum_{j=0}^{N-1}T_j(k)\exp(i2\pi jn/N),\quad n=1,\ldots,N. \tag{23}$$

As shown above, a $k$ eigenvalue occurs whenever $\lambda_n(k)=1$. Note also that $\lambda_{-n}(k)=\lambda_n(k)$, since $T_{-j}(k)=T_j(k)$.

Equation (23) enables us to calculate the $k$ eigenvalues to high accuracy. In fact, with $N$ chosen to be 100, the results based on Eq. (23) were found to agree with the results obtained from Eq. (16) to six significant figures (for the lowest 15 distinct eigenvalues). This is not entirely surprising since if we substitute $T_j(k)$ given by Eq. (20) in Eq. (23), with $\theta_j=j(2\pi/N)$, replace the sum over $j$ by an integral over $\theta$, and use the orthonormality of the functions $\{\exp(il\theta)/(2\pi)^{1/2}\}$, we find that $\lambda_n(k)$ is equal to $\lambda_l(k)$ given by Eq. (18). Thus it is appropriate to label the eigenvalue curves by $l$ and write Eq. (23) as

$$\lambda_l(k)=\lambda_{-l}(k)=\sum_{j=0}^{N-1}T_j(k)\exp(il\theta_j),\quad l=0,1,\ldots, \tag{24}$$

where $T_j(k)$ is given by Eq. (20) with $\Delta\theta=2\pi/N$.

## III. SEMICLASSICAL APPROXIMATIONS OF THE GREEN FUNCTION

Up to this point we have been considering the exact quantum-mechanical Green function, Eqs. (5) and (6). Our main interest is in exploring what happens when this exact Green function is replaced by semiclassical Green functions corresponding to different approximations. The semiclassical approximations described below are similar in many respects to those obtained by Primack *et al.* [27] in their study of diffractive effects in the Sinai billiard. They are based on the mathematical expansions described in great detail by Nussenzveig [38].

To obtain the semiclassical approximations, we first use the Poisson summation formula to rewrite Eqs. (5) and (6) (with $\theta$ now denoting $\theta'-\theta$) as [27]

$$G(\mathbf{r},\mathbf{r}';k)=\sum_{M=-\infty}^{\infty}-\frac{im}{4\hbar^2}\int_{-\infty}^{\infty}dl[H_l^-(kr_<)+S_l(ka)H_l^+(kr_<)]H_l^+(kr_>)\times\exp(il\theta+i2\pi Ml), \tag{25}$$

where, as before, $S_l(ka)=-H_l^-(ka)/H_l^+(ka)$. Following Primack *et al.* [27] we consider only the term $M=0$ in the summation over $M$, which they found to make the dominant contribution in their study of the Sinai billiard. In what follows we require $G(\theta_0,\theta_j;k)$ with $r_<=r_>=R$. Denoting the contribution to the Green function from the term $M=0$ by $G_0(\theta;k)$, where $\theta=\theta_j-\theta_0$, we have,

$$G_0(\theta;k)=-\frac{im}{4\hbar^2}\int_{-\infty}^{\infty}dl[H_l^-(kR)+S_l(ka)H_l^+(kR)]\times H_l^+(kR)\exp(il\theta). \tag{26}$$

Relative to the position $\theta=0$, the outer circle of the annulus is divided into three regions: the illuminated region, the penumbra, and the shadow region (see Fig. 2). From the symmetry of Fig. 2, it suffices to consider $\theta$ to be in the interval $(0,\pi)$. In the Appendix we use the conditions on the validity of the approximations in the different regions to determine the boundary points. The boundary point between the illuminated region and the penumbra is found to be

$$\theta_{\rm ip}=\cos^{-1}\left(\frac{ka+(ka)^{1/3}}{kR}\right)+\cos^{-1}(a/R)-(ka)^{-1/3}, \tag{27}$$

while the point separating the penumbra from the shadow region is

$$\theta_{\rm ps}=2\cos^{-1}(a/R)+(3/2)(ka)^{-1/3}. \tag{28}$$

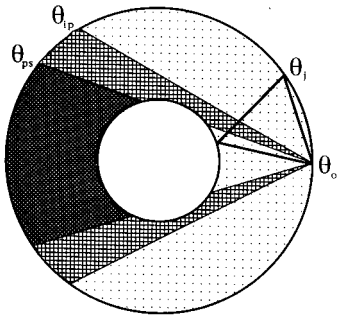


FIG. 2. The annulus billiard showing the illuminated, penumbra, and shadow regions relative to $\theta_0=0$. The direct and reflected paths from $\theta_0$ to $\theta_j$ are shown in the illuminated region. $\theta_{\rm ip}$ is the boundary between the illuminated region and the penumbra. $\theta_{\rm ps}$ is the boundary between the penumbra and the shadow region.

When the angle $\theta$ lies in the illuminated region, the leading terms resulting from Nussenzveig's analysis are, for $\theta \leqslant \theta_{\rm ip}$,

$$G_0^{(i)}(\theta;k) = -\frac{e^{i\pi/4}m}{(2\pi)^{1/2}\hbar^2}\left[\frac{e^{ikL_1}}{(kL_1)^{1/2}} - \frac{e^{ikL_2}}{(kL_2)^{1/2}} \times \left(\frac{R\cos\alpha - L_2/2}{R\cos\alpha}\right)^{1/2}\right], \tag{29}$$

where $L_1$ is the length of the direct path from $(R,0)$ to $(R,\theta)$, and $L_2$ is the length of the path reflected from the inner circle, as shown in Fig. 2. In Eq. (29), $\alpha$ is the angle between the reflected ray and the inward normal at $(R,0)$ or $(R,\theta)$. One can see that when the reflected path becomes tangent to the inner circle, the square-root factor involving $\alpha$ goes to zero. Note that the negative sign preceding the second term in Eq. (29) can be interpreted as resulting from a phase change of $\pi$ on reflection from the inner circle.

When $\theta$ lies in the penumbra, the leading terms in the expansions yield the result, for $\theta_{\rm ip} \leqslant \theta \leqslant \theta_{\rm ps}$,

$$G_0^{(p)}(\theta;k) = -\frac{e^{i\pi/4}m}{(2\pi)^{1/2}\hbar^2}\left[\frac{e^{ikL}}{(kL)^{1/2}}\frac{F(\infty)-F(\nu)}{(2i)^{1/2}}\right] + \frac{(ka)^{1/3}C}{2\pi k L_r}\exp[ik(2L_r \pm a\gamma_0)], \tag{30}$$

where $F(\nu)=\int_0^\nu \exp(i\pi\tau^2/2)d\tau$ and $\nu=(kL/\pi)^{1/2}[\sin^{-1}(a/R)-(\pi/2-\theta/2)]$. According to Nussenzveig [38] and Primack *et al.* [27], the constant $C$ has the value $C=0.996\,15\exp(i\pi/3)$. The first term in Eq. (30), which is the contribution from the direct path of length $L$, is the same as the first term of Eq. (29) multiplied by the *Fresnel factor* $[F(\infty)-F(\nu)]/(2i)^{1/2}$. This factor varies smoothly between 0 and 1, tending to unity as $\theta$ approaches the border of the illuminated region, and tending to zero as $\theta$ approaches the shadow boundary. [At the angle specifying the geometrical shadow, $\theta=2\cos^{-1}(a/R)$, $\nu$ is zero and the Fresnel factor is equal to $\frac{1}{2}$.] The second term in Eq. (30) is the *glancing* contribution, which depends on whether $\theta$ lies outside or inside the region of the geometrical shadow. Here $L_r=(R^2-a^2)^{1/2}$, and the $-$ and $+$ signs apply to the upper and lower cases shown in Fig. 3, respectively. In the upper case, the path length appearing in the exponential is shortened by the arc length $a\gamma_0$ between the points of tangency. In the lower case, the path length includes the distance $a\gamma_0$ that the diffracted ray creeps along the surface of the disk. Equation (30), which we have derived independently [39], is exactly the same as the result obtained by Primack *et al.* [27].

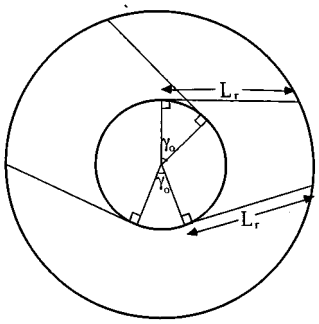


FIG. 3. Two diffractive paths in the penumbra region of the annulus billiard. In the upper situation, the effective length of the diffractive path is $2L_r - a\gamma_0$. In the lower case it is $2L_r + a\gamma_0$.

Finally, when $\theta$ lies in the shadow region, Nussenzveig's analysis leads to the following form for the Green function, for $\theta_{\rm ps} \leqslant \theta \leqslant \pi$:

$$G_0^{(s)}(\theta;k) = -\frac{e^{i\pi/3}m}{2\pi\hbar^2}(ka/2)^{1/3}\sum_n \frac{(k^2R^2-l_n^2)^{-1/2}}{[\mathrm{Ai}'(-x_n)]^2} \times \exp\{i[2(k^2R^2-l_n^2)^{1/2} - 2l_n\cos^{-1}(l_n/kR) + l_n\theta]\}, \tag{31}$$

where $-x_n$ is the $n$th zero of the Airy function $\mathrm{Ai}(-x)$, $\mathrm{Ai}'(-x_n)$ is the derivative of the Airy function at $-x_n$, and $l_n = ka + (ka/2)^{1/3}x_n e^{i\pi/3}$. Although this expression looks complicated, one can show that the real part of the exponent of the exponential function is equal to $-(\sqrt{3}/2)(ka/2)^{1/3}\gamma_0 x_n$, where $\gamma_0=\theta-2\cos^{-1}(a/R)$ is the creeping angle, similar to $\gamma_0$ in the lower part of Fig. 2. Since $x_n$ is positive and increases as $n$ increases ($x_1=2.338$, $x_2=4.088$, $x_3=5.521$, ..., $x_{10}=12.829$, ...), the contributions to the sum over $n$ in Eq. (31) will decrease fairly rapidly as long as $(ka)^{1/3}\gamma_0$ is greater than unity. Thus the condition $\gamma_0 > (ka)^{-1/3}$ will be assumed to hold in the shadow region, as stated in the Appendix. Then the sum in Eq. (31) can be limited to the first few poles of $S_l(ka)$ nearest the real axis in the complex $l$ plane. Equation (31) is essentially the same as the contributions from creeping waves described by Vattay, Wirzba, and Rosenqvist [16].

In addition to the path we have just described, there are other diffractive paths containing longer creeping arcs which will contribute, in principle, to the semiclassical Green function in all three regions. For example, for $\theta$ still in the range $(0,\pi)$, there is a somewhat longer diffractive path to the shadow region which creeps around an arc on the opposite side of the inner circle. The (positive) value of the creeping angle for this path is $\gamma_0=2\pi-2\cos^{-1}(a/R)-\theta$, which has its smallest value when $\theta=\pi$. This path, and other even

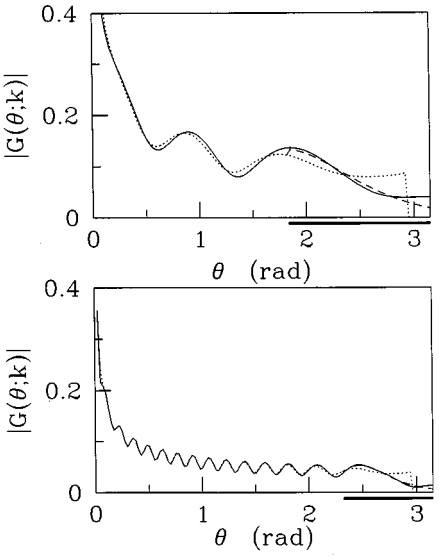


FIG. 4. $|G(\theta;k)|$ as a function of $\theta$, for $a=0.1R$. The solid curves are the exact Green function, calculated from Eqs. (5) and (6). The dotted curves are the Bogomolny semiclassical Green function, as explained in the text. The dashed curves are the semiclassical Green function calculated from Eqs. (30) and (31), which describe the diffractive paths in the penumbra and shadow regions. Upper plot: eigenvalue $k=9.936$ calculated with $N=200$; lower plot: eigenvalue $k=49.959$ calculated with $N=250$. Here $k$ is related to the energy by $E=\hbar^2k^2/(2m)$, in units in which $\hbar=m=1$. $N$ is the dimension of the $T$ matrix, which is equal to the number of cells on the PSS.

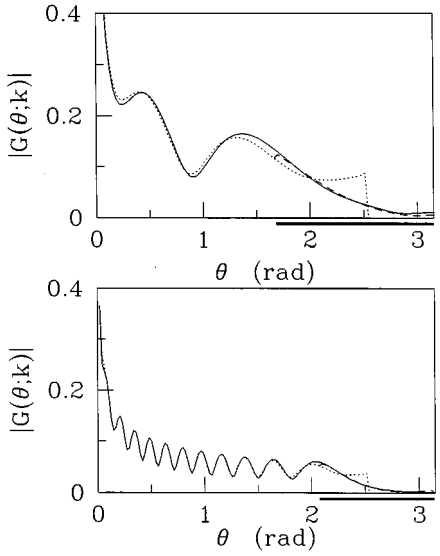


FIG. 5. The same as Fig. 4 for $a=0.3R$. Upper plot: eigenvalue $k=9.939$ calculated with $N=200$; lower plot: eigenvalue $k=49.959$ calculated with $N=300$.

longer paths, which have their mathematical origin in the sum over $M$ in Eq. (25), can be included in the semiclassical Green function (in any region) by adding contributions like Eq. (31), with $\theta$ replaced by $\theta+2\pi M$, $M=\pm1,\pm2,\ldots$. However, we have neglected all such contributions in the calculations that we are about to describe, since it was found that when the shadow region exists, the contribution $G_0^{(s)}(\theta;k)$ from the *shortest* creeping path became negligible well before $\theta=\pi$.

We are now in a position to consider different semiclassical approximations to the Green function, and compare them with the exact Green function. In Figs. 4–6, which correspond to the radius $a$ of the inner circle being equal to $0.1R$, $0.3R$, and $0.5R$, respectively, the solid curves show the modulus of the exact Green function, calculated as described in Sec. II. Plots for two different $k$-eigenvalues (close to 10 and 50) are shown in each case. The solid bar under the $\theta$ axis indicates the penumbra region in each plot, extending from $\theta_{\rm ip}$ given by Eq. (27) to $\theta_{\rm ps}$ given by Eq. (28).

The simplest semiclassical approximation consists of $G_0^{(i)}(\theta;k)$ given by Eq. (29) being employed, not only throughout the illuminated region, but also into the penumbra region, until the straight line joining $(R,0)$ to $(R,\theta)$ is tangent to the inner circle. We have shown that this expression is exactly the same as Bogomolny's semiclassical Green function on the Poincaré surface of section, chosen to be the outer circle of the annulus [see Eq. (3.10) of Ref. [28]]. Thus, this approximation is equivalent to Bogomolny's Poincaré map from $(R,0)$ to $(R,\theta)$ involving two classical trajectories, the direct one and the one reflected from the inner circle. The Green function is assumed to be zero in the region of the geometrical shadow. This approximation, which we shall call the *Bogomolny semiclassical approximation*, is shown as the dotted curves in Figs. 4–6. For $k$ eigenvalues close to 10 and 50, the dotted curves are very close to the exact Green function throughout the region $0<\theta<\theta_{\rm ip}$, but there are noticeable differences in the penumbra region where Eq. (29) is not valid.

The modifications to the penumbra and shadow regions, calculated from Eqs. (30) and (31), are shown as the dashed curves in Figs. 4–6. [The sum over $n$ in Eq. (31) was taken over ten terms.] It may be seen that the agreement between these curves and the exact Green function is very good. It is satisfying, though somewhat surprising, that keeping only the leading terms of Nussenzveig's expansions for the pen-

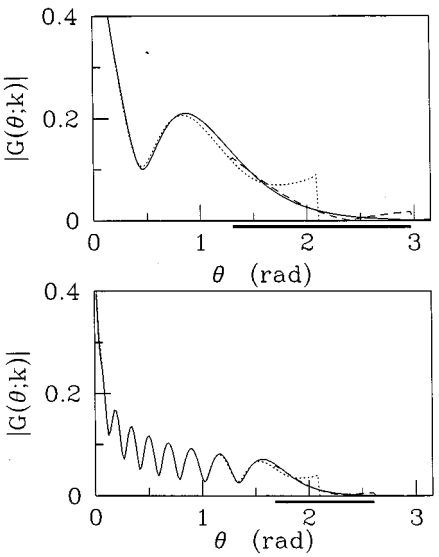


FIG. 6. The same as Fig. 4 for $a=0.5R$. Upper plot: eigenvalue $k=10.189$ calculated with $N=250$; lower plot: eigenvalue $k=49.999$ calculated with $N=350$.

umbra, Eq. (30), accounts for almost all of the difference between Bogomolny's semiclassical approximation and the exact Green function. We also note that in Fig. 6, where a shadow region exists, the contribution given by Eq. (31) is too small to be visible on the plots.

## IV. TRANSFER OPERATOR INCLUDING DIFFRACTIVE PATHS

We now turn to the calculation of the transfer operator in the two approximations described in Sec. III. Guided by Bogomolny's route from the semiclassical Green function to the transfer operator [28], and by Eqs. (12) and (13), we postulate the semiclassical transfer operator to be

$$T_{\rm sc}(\theta;k) = -\frac{i\hbar^2}{m}\sum_{\rm paths}(kR\cos\phi)G_{\rm sc}(\theta;k), \qquad (32)$$

where the sum is over different geometrical paths from $(R,0)$ to $(R,\theta)$. [In the notation of Eq. (1), $\theta$ is $|\theta''-\theta'|$.] Here $\phi$ is the angle between the inward normal to the outer circle and the direction of the geometrical path immediately after being reflected from the outer circle at $(R,0)$ or at $(R,\theta)$. In Eq. (32), $G_{\rm sc}(\theta;k)$ is a semiclassical Green function, which may have different forms in the illuminated, penumbra, and shadow regions. As in Bogomolny's theory [28], the direct zero-length trajectories corresponding to $\theta=0$ are excluded from $G_{\rm sc}(\theta;k)$ in Eq. (32), but $G_{\rm sc}(0;k)$ includes the classical trajectory along the radial direction which returns to $(R,0)$ after bouncing off the inner circle. Note that $T_{\rm sc}(\theta;k)$ requires information only about the classical trajectories and diffractive paths.

As in the case of the exact $T$ matrix, Eqs. (19) and (20), we construct a finite approximation to the semiclassical $T$ operator by dividing the Poincaré surface of section into $N$ cells of width $\Delta\theta=2\pi/N$. The $N$ distinct matrix elements are

$$T_j(k) = T(\theta_j,\theta_0;k)\Delta\theta = -\frac{i\hbar^2}{m}\sum_{\rm paths}(kR\cos\phi_j)G_{\rm sc}(\theta_j;k)\Delta\theta, \qquad (33)$$

where $\phi_j$ is the angle between the inward normal to the outer circle and the particular classical or diffractive path involved in going from $\theta_0=0$ to $\theta_j$. Equations (24) and (33) enable us to calculate the energy eigenvalues using different semiclassical approximations for $G_{\rm sc}(\theta_j;k)$.

Figures 7–9 show $|T(\theta;k)|$ for the same cases as the earlier plots of $|G(\theta;k)|$. As before, the solid bar under the $\theta$ axis indicates the extent of the penumbra in each case. The solid curves are the exact quantum-mechanical transfer operator calculated from Eq. (21), with $g_l(R,R;k)$ given by Eq. (6). The dotted curves correspond to Bogomolny's semiclassical approximation. They were calculated from Eq. (32) by replacing $G_{\rm sc}(\theta;k)$ by the semiclassical approximation $G_0^{(i)}(\theta;k)$ for the illuminated region, Eq. (29), employed from $\theta=0$ to the angle at which the straight line joining $(R,0)$ to $(R,\theta)$ is tangent to the inner circle. Beyond this angle the Green function was set equal to zero. This approximation is, in fact, exactly the same as that given by Eq. (1),

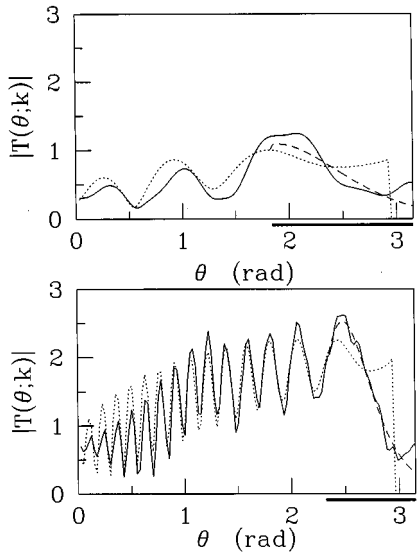


FIG. 7. $|T(\theta;k)|$ as a function of $\theta$, for $a=0.1R$. The solid curves are the exact transfer operator, calculated from Eq. (21). The dotted curves are the Bogomolny semiclassical approximation, as explained in the text. The dashed curves are the semiclassical approximation calculated from Eq. (32) using Eqs. (30) and (31), which describe the diffractive paths in the penumbra and shadow regions. Upper plot: eigenvalue $k=9.936$ calculated with $N=250$; lower plot: eigenvalue $k=49.959$ calculated with $N=250$.

constructed using purely classical trajectories. Finally, the dashed curves in the figures were constructed from Eq. (32) using the semiclassical approximations (29)–(31) for $G_0^{(i)}(\theta;k)$, $G_0^{(p)}(\theta;k)$, and $G_0^{(s)}(\theta;k)$ in the three regions.

The most striking feature of Figs. 7–9 is the large oscillations occurring in the illuminated region of each plot. These come from the interference between the two terms in Eq. (29), the direct term and the reflected term. From Eqs. (29) and (32) the contribution to the $T$ operator from the direct path is

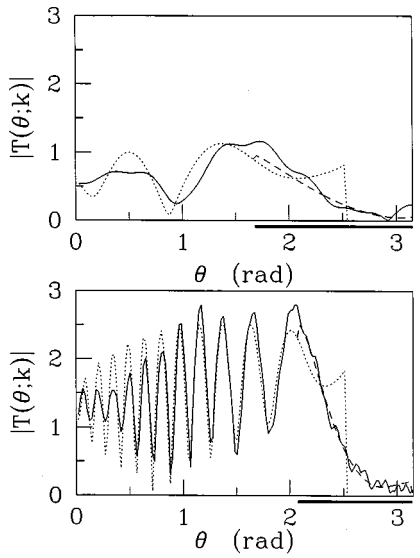


FIG. 8. The same as Fig. 7 for $a=0.3R$. Upper plot: eigenvalue $k=9.939$ calculated with $N=200$; lower plot: eigenvalue $k=49.959$ calculated with $N=300$.

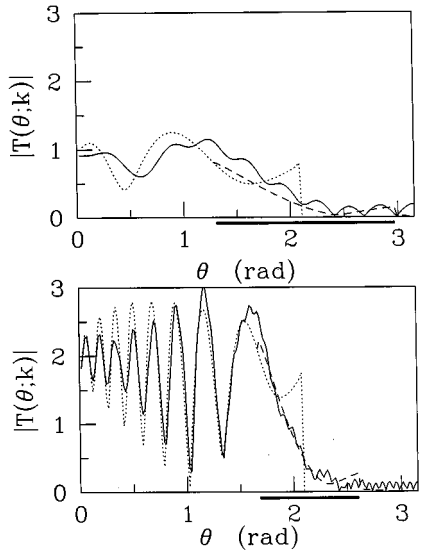


FIG. 9. The same as Fig. 7 for $a=0.5R$. Upper plot: eigenvalue $k=10.189$ calculated with $N=250$; lower plot: eigenvalue $k=49.999$ calculated with $N=350$.

$$T_d^{(i)}(\theta;k)=\frac{e^{i3\pi/4}}{2\pi^{1/2}}[kR\sin(\theta/2)]^{1/2}\exp[i2kR\sin(\theta/2)]. \tag{34}$$

In the upper part of Fig. 10, the real part of this expression is plotted as a function of $\theta$, for the case shown in the lower part of Fig. 9. One can see that the factor $[\sin(\theta/2)]^{1/2}$ causes the amplitude of the oscillations to increase gradually as $\theta$ goes from 0 to $\theta_{\rm ip}$, the penumbra boundary. Similarly, the contribution to the $T$ operator from the reflected path is,

$$T_r^{(i)}(\theta;k)=-\frac{e^{i3\pi/4}}{2\pi^{1/2}}(kR\cos\alpha)^{1/2}\frac{(R\cos\alpha-L_2/2)^{1/2}}{(L_2/2)^{1/2}}e^{ikL_2}, \tag{35}$$

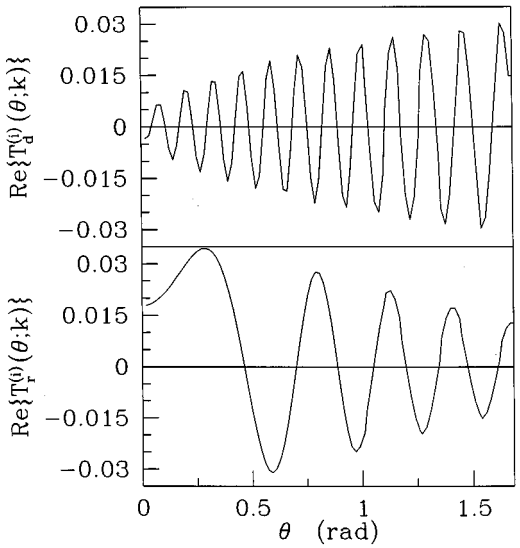


FIG. 10. Comparison of the two terms contributing to the semiclassical transfer operator in the illuminated region. The upper curve is the real part of the direct contribution given by Eq. (34). The lower curve is the real part of the reflected contribution given by Eq. (35).

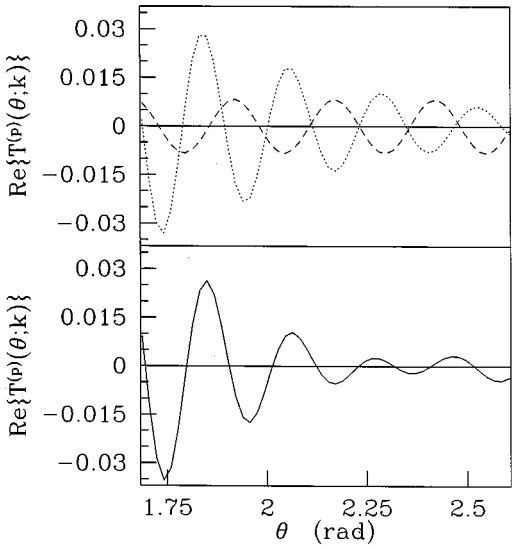


FIG. 11. Comparison of the two terms contributing to the semiclassical transfer operator in the penumbra. The dotted curve is the real part of the direct contribution, given by Eq. (34) multiplied by the Fresnel factor. The dashed curve is the real part of the glancing contribution, given by Eq. (32) with the second term of (30) substituted for $G_{\rm sc}(\theta;k)$. In the lower part of the figure, the solid curve is the sum of these two contributions.

where $L_2/2=[R^2+a^2-2aR\cos(\theta/2)]^{1/2}$. In Eq. (35), as in Eq. (29), $\alpha$ is the angle between the inward normal to the outer circle and the reflected path at $(R,0)$ or $(R,\theta)$; it is the same as the angle $\phi$ in Eq. (32). The real part of Eq. (35) is plotted as a function of $\theta$ in the lower part of Fig. 10. The amplitude factor in this expression is a maximum at $\theta=0$ (where $\alpha=0$), and steadily decreases as $\theta$ goes from 0 to $\theta_{\rm ip}$. Figure 10 makes it plausible that the eight oscillations in $|T^{(i)}(\theta;k)|$ in the lower part of Fig. 9 result from interference between the 12 oscillations of the direct term and the four oscillations of the reflected term in the illuminated region. (Note that the jagged peaks and troughs in the upper part of Fig. 10 are due to the limited number of points used to plot the curve.)

We have performed a similar comparison of the contributions to $T_{\rm sc}^{(p)}(\theta;k)$ in the penumbra, again for the case shown in the lower part of Fig. 9. The results are shown in Fig. 11. In the upper part of the figure, the dotted curve is the real part of Eq. (32) coming from the first term of Eq. (30). This has the same form as Eq. (34) for the illuminated region, multiplied by the Fresnel factor $[F(\infty)-F(\nu)]/(2i)^{1/2}$. The Fresnel factor causes the oscillations to decrease in amplitude as $\theta$ goes through the penumbra from $\theta_{\rm ip}$ to $\theta_{\rm ps}$. On the same plot the dashed curve is the real part of Eq. (32) coming from the second term of Eq. (30), calculated with $\cos\phi=L_r/R$. It oscillates with constant amplitude and almost-constant wavelength. (The term $\pm a\gamma_0$ in the exponential function, which goes smoothly from a negative to a positive value as $\theta$ increases through the penumbra, is small compared to $2L_r$.) Close to the shadow boundary, the two contributions may be seen to be comparable in magnitude. In the lower part of Fig. 11 we have plotted the sum of these contributions to $T_{\rm sc}^{(p)}(\theta;k)$.

There are other points of interest in Figs. 7–9. First, there

is the obvious feature that, in the penumbra, the semiclassical approximation which properly describes diffractive effects in this region is close to the exact curves, particularly for the higher-$k$ eigenvalues. In contrast, the dotted curves, calculated from Bogomolny's semiclassical approximation, display a discontinuity at the angle of the geometrical shadow boundary. It is also noteworthy that in the illuminated region, for angles $\theta$ up to about 1 rad, the amplitude of the oscillations of the semiclassical transfer operator is larger than that of the exact transfer operator, although the number of oscillations and the phases are in good agreement. Finally, we note that the exact transfer operator displays small oscillations of relatively short wavelength, most clearly visible in Figs. 8 and 9. We attribute these to the cutoff in the sum over $l$ in Eq. (21) at $|l|=kR$. We suspect these oscillations may be physical since the energy eigenvalues calculated from Eqs. (20) and (23) agree with the exact quantum energies to six significant figures, as was mentioned near the end of Sec. II.

## V. SEMICLASSICAL AND EXACT ENERGY EIGENVALUES

It remains to present the results of calculations of the energy eigenvalues in the two different semiclassical approximations described above, and compare them with the exact energy eigenvalues. As a standard for comparison, we also give the energy eigenvalues calculated using the simple Einstein-Brillouin-Keller quantization scheme.

In the discussion that follows it will be advantageous to use *scaled* energies $\widetilde{E}$, such that the mean separation between the quantum energy levels (taking degeneracies into account) is unity. The scaled energies are defined to be

$$\widetilde{E}=N_{\mathrm{TF}}(E)=\frac{m(R^2-a^2)}{2\hbar^2}E-\left(\frac{m}{2\hbar^2}\right)^{1/2}(R+a)E^{1/2}. \tag{36}$$

Here $N_{\mathrm{TF}}(E)$ is the Thomas-Fermi approximation to the exact staircase function $N(E)$, the number of quantum states having energy less than $E$. It was calculated by a method similar to that described in a well-known paper by Kac [40]. The first term is determined by the area of the billiard domain, while the second term depends on the length of the boundary (both circles). The scaled quantum energy eigenvalues $\widetilde{E}_{ln}$, related to the unscaled energy eigenvalues $E_{ln}$ by Eq. (36), have a mean separation of unity. In Fig. 12 the solid curve is the staircase function constructed from the exact quantum energy eigenvalues up to $E=200$, taking degeneracies into account. The dashed line, which is a plot of $N_{\mathrm{TF}}(E)$ given by Eq. (36), is clearly an excellent approximation to $N(E)$ over this energy range.

The results for the scaled energy eigenvalues, calculated by means of Eqs. (24), (33), and (36), are shown in Tables I–III, which list the first 30 distinct energy levels for the cases $a=0.1R$, $a=0.3R$, and $a=0.5R$, respectively. The results in columns 4, 5, and 6 of the tables were calculated from Eq. (24), with $N$ chosen to be 100. Since the eigenvalue curve $\lambda_0(k)$ for $l=0$ is nondegenerate, while for $l\neq 0$ the curves $\lambda_l(k)$ and $\lambda_{-l}(k)$ are degenerate, only the distinct eigenvalues corresponding to $l=0,1,2,\ldots$ are listed in the tables. The first column gives the $l$ value of the curve $\lambda_l(k)$, and the second column gives the *crossing number*,

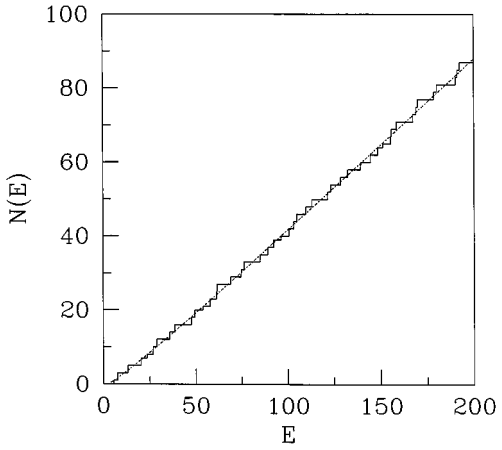


FIG. 12. Comparison of the exact staircase function $N(E)$ (solid curve) with the Thomas-Fermi approximation $N_{\mathrm{TF}}(E)$ (dashed curve) given by Eq. (36).

TABLE I. Comparison of the semiclassical scaled energy eigenvalues, in three different approximations, with the exact scaled energy eigenvalues. Case $a=0.1R$.

| $l$ | $n$ | $\widetilde{E}_{ln}^{\mathrm{sc,EBK}}$ | $\widetilde{E}_{ln}^{\mathrm{sc,Bog}}$ | $\widetilde{E}_{ln}^{\mathrm{sc,diff}}$ | $\widetilde{E}_{ln}^{\mathrm{exact}}$ |
|---|---|---|---|---|---|
| 0 | 1 | 1.096 | 0.633 | 0.966 | 0.895 |
| 1 | 1 | 1.477 | 1.690 | 1.916 | 1.676 |
| 2 | 1 | 3.633 | 3.760 | 3.858 | 3.717 |
| 3 | 1 | 6.475 | 6.350 | 6.606 | 6.567 |
| 0 | 2 | 8.223 | 9.432 | 7.988 | 7.867 |
| 1 | 2 | 8.269 | 9.128 | 9.674 | 9.268 |
| 4 | 1 | 9.965 | 9.620 | 10.083 | 10.078 |
| 2 | 2 | 12.844 | 13.260 | 13.439 | 13.052 |
| 5 | 1 | 14.083 | 13.802 | 14.241 | 14.218 |
| 3 | 2 | 18.143 | 18.154 | 18.398 | 18.226 |
| 6 | 1 | 18.811 | 18.874 | 19.088 | 18.970 |
| 0 | 3 | 21.382 | 23.803 | 21.650 | 20.946 |
| 1 | 3 | 23.788 | 22.123 | 23.023 | 22.681 |
| 4 | 2 | 24.136 | 23.588 | 24.276 | 24.216 |
| 7 | 1 | 24.139 | 24.715 | 24.491 | 24.322 |
| 2 | 3 | 26.966 | 27.963 | 28.263 | 27.648 |
| 8 | 1 | 30.058 | 31.089 | 30.438 | 30.266 |
| 5 | 2 | 30.805 | 29.962 | 30.858 | 30.894 |
| 3 | 3 | 34.702 | 35.044 | 35.279 | 34.853 |
| 9 | 1 | 36.561 | 37.538 | 36.946 | 36.794 |
| 6 | 2 | 38.134 | 37.398 | 38.187 | 38.231 |
| 0 | 4 | 40.572 | 43.358 | 41.843 | 40.089 |
| 1 | 4 | 42.944 | 40.856 | 42.116 | 42.022 |
| 4 | 3 | 43.151 | 42.672 | 43.458 | 43.229 |
| 10 | 1 | 43.641 | 43.822 | 44.007 | 43.900 |
| 7 | 2 | 46.109 | 45.793 | 46.280 | 46.217 |
| 2 | 4 | 45.985 | 47.999 | 48.456 | 47.741 |
| 11 | 1 | 51.294 | 50.991 | 51.581 | 51.579 |
| 5 | 3 | 52.297 | 51.151 | 52.400 | 52.373 |
| 8 | 2 | 54.721 | 55.001 | 55.014 | 54.839 |
| | | 0.508 | 0.991 | 0.425 | |

TABLE II. The same as Table I for the case $a=0.3R$.

| $l$ | $n$ | $\tilde{E}_{ln}^{\mathrm{sc,EBK}}$ | $\tilde{E}_{ln}^{\mathrm{sc,Bog}}$ | $\tilde{E}_{ln}^{\mathrm{sc,diff}}$ | $\tilde{E}_{ln}^{\mathrm{exact}}$ |
|---|---|---|---|---|---|
| 0 | 1 | 1.665 | 2.480 | 1.915 | 1.561 |
| 1 | 1 | 2.205 | 1.923 | 2.153 | 1.979 |
| 2 | 1 | 2.603 | 3.265 | 3.327 | 3.252 |
| 3 | 1 | 5.035 | 4.935 | 5.470 | 5.372 |
| 4 | 1 | 8.069 | 7.866 | 8.293 | 8.265 |
| 5 | 1 | 11.683 | 11.613 | 11.859 | 11.834 |
| 0 | 2 | 12.495 | 12.864 | 13.083 | 12.347 |
| 1 | 2 | 13.137 | 13.944 | 13.355 | 12.939 |
| 2 | 2 | 15.128 | 15.191 | 14.935 | 14.727 |
| 6 | 1 | 15.861 | 15.685 | 16.035 | 16.011 |
| 3 | 2 | 15.269 | 17.357 | 17.885 | 17.730 |
| 7 | 1 | 20.593 | 20.179 | 20.805 | 20.758 |
| 4 | 2 | 20.590 | 21.106 | 22.054 | 21.921 |
| 8 | 1 | 25.869 | 25.658 | 26.204 | 26.055 |
| 5 | 2 | 26.536 | 26.789 | 27.337 | 27.202 |
| 9 | 1 | 31.683 | 31.938 | 32.072 | 31.892 |
| 0 | 3 | 32.489 | 31.110 | 32.635 | 32.326 |
| 1 | 3 | 33.169 | 34.115 | 33.681 | 32.980 |
| 6 | 2 | 33.092 | 33.130 | 33.529 | 33.423 |
| 2 | 3 | 35.235 | 36.087 | 35.760 | 34.951 |
| 10 | 1 | 38.029 | 38.484 | 38.500 | 38.261 |
| 3 | 3 | 38.770 | 39.976 | 38.604 | 38.270 |
| 7 | 2 | 40.245 | 39.619 | 40.439 | 40.432 |
| 4 | 3 | 43.953 | 41.987 | 43.199 | 42.967 |
| 11 | 1 | 44.903 | 45.238 | 45.400 | 45.159 |
| 8 | 2 | 47.985 | 47.020 | 48.135 | 48.122 |
| 5 | 3 | 45.805 | 48.110 | 49.163 | 49.045 |
| 12 | 1 | 52.300 | 52.945 | 52.721 | 52.580 |
| 9 | 2 | 56.305 | 55.632 | 56.491 | 56.430 |
| 6 | 3 | 54.651 | 56.145 | 56.688 | 56.447 |
| | | 0.908 | 0.730 | 0.299 | |

TABLE III. The same as Table I for the case $a=0.5R$.

| $l$ | $n$ | $\tilde{E}_{ln}^{\mathrm{sc,EBK}}$ | $\tilde{E}_{ln}^{\mathrm{sc,Bog}}$ | $\tilde{E}_{ln}^{\mathrm{sc,diff}}$ | $\tilde{E}_{ln}^{\mathrm{exact}}$ |
|---|---|---|---|---|---|
| 0 | 1 | 2.690 | 2.943 | 3.060 | 2.630 |
| 1 | 1 | 2.947 | 3.360 | 3.228 | 2.869 |
| 2 | 1 | 3.744 | 4.424 | 3.738 | 3.595 |
| 3 | 1 | 5.143 | 4.590 | 5.048 | 4.835 |
| 4 | 1 | 5.032 | 6.587 | 6.784 | 6.613 |
| 5 | 1 | 7.757 | 8.416 | 9.060 | 8.943 |
| 6 | 1 | 10.951 | 11.464 | 11.915 | 11.823 |
| 7 | 1 | 14.604 | 14.837 | 15.283 | 15.243 |
| 8 | 1 | 18.709 | 18.485 | 19.164 | 19.186 |
| 0 | 2 | 20.184 | 21.514 | 20.346 | 20.107 |
| 1 | 2 | 20.500 | 20.275 | 20.715 | 20.416 |
| 2 | 2 | 21.451 | 21.124 | 21.849 | 21.345 |
| 3 | 2 | 23.050 | 23.921 | 23.706 | 22.904 |
| 9 | 1 | 23.259 | 23.192 | 23.515 | 23.630 |
| 4 | 2 | 25.318 | 26.349 | 25.789 | 25.103 |
| 5 | 2 | 28.282 | 29.769 | 28.391 | 27.956 |
| 10 | 1 | 28.249 | 27.873 | 28.478 | 28.558 |
| 6 | 2 | 31.979 | 31.820 | 31.663 | 31.476 |
| 11 | 1 | 33.676 | 33.173 | 33.892 | 33.952 |
| 7 | 2 | 36.458 | 35.777 | 35.867 | 35.672 |
| 12 | 1 | 39.535 | 39.319 | 39.788 | 39.800 |
| 8 | 2 | 41.791 | 39.803 | 40.833 | 40.549 |
| 13 | 1 | 45.823 | 45.296 | 46.067 | 46.090 |
| 9 | 2 | 42.714 | 45.237 | 46.363 | 46.102 |
| 10 | 2 | 49.787 | 51.756 | 52.527 | 52.322 |
| 0 | 3 | 52.483 | 51.527 | 52.988 | 52.400 |
| 1 | 3 | 52.818 | 53.368 | 53.052 | 52.732 |
| 14 | 1 | 52.538 | 52.174 | 52.898 | 52.815 |
| 2 | 3 | 53.826 | 54.517 | 53.952 | 53.729 |
| 3 | 3 | 55.510 | 56.164 | 55.748 | 55.396 |
| | | 0.940 | 0.747 | 0.319 | |

i.e., the count for the number of times the curve $\lambda_l(k)$ has crossed the real axis at $+1$, as illustrated in Fig. 1. Column 4 lists the scaled energy eigenvalues calculated in Bogomolny's semiclassical approximation, described above. The fifth column lists the semiclassical scaled energy eigenvalues calculated including diffractive paths in the penumbra and shadow regions. Finally, column 6 gives the exact quantum-mechanical scaled energies calculated from Eqs. (20) and (24). At the bottom of columns 4 and 5 we give the root-mean-square (rms) deviation of the scaled semiclassical energy eigenvalues listed in that column from the exact scaled energies. These numbers reflect what is clearly evident in the tables, namely, that in comparison with Bogomolny's semiclassical approximation, the inclusion of diffractive effects brings the energy eigenvalues into much better agreement with the exact energies. In fact, the rms deviation is reduced by almost 60% in each case.

In judging the relative merit of the two semiclassical approximations described above, it is helpful to compare them with a much simpler semiclassical approximation, namely, the Einstein-Brillouin-Keller (EBK) quantization scheme. (See, for example, Ref. [2], p. 214.) The EBK energy eigenvalues for the annulus billiard are obtained by quantizing the two independent action integrals,

$$S_\theta=\int_0^{2\pi} p_\theta d\theta=2\pi L=lh, \quad l=0,1,2,\ldots, \tag{37}$$

where $L$ is the constant classical angular momentum, and

$$S_r=\oint p_r dr=2\int_{r_{\min}}^{R}(2mE-l^2\hbar^2/r^2)^{1/2}dr$$
$$=(n-1+\beta/4)h, \quad n=1,2,\ldots. \tag{38}$$

The lower limit of this radial integral is either the classical turning point $r_1=l\hbar/(2mE)^{1/2}$, or the radius $a$ of the inner circle of the annulus, whichever is larger. When $r_1>a$, the value of $\beta$ is 3, corresponding to a ''soft'' turnaround caused by the $l^2\hbar^2/r^2$ potential. On the other hand, when $r_1\leqslant a$, the value of $\beta$ is 4, since in this case the particle makes a hard-wall collision with the inner circle of the annulus. Note that the integer on the right-hand side of Eq. (38) has been written as $n-1$, with $n=1,2,\ldots$, in order that $n$ will correspond to the crossing number defined above. Working out the integral in Eq. (38) for given $l$ and $n$ leads to an equation

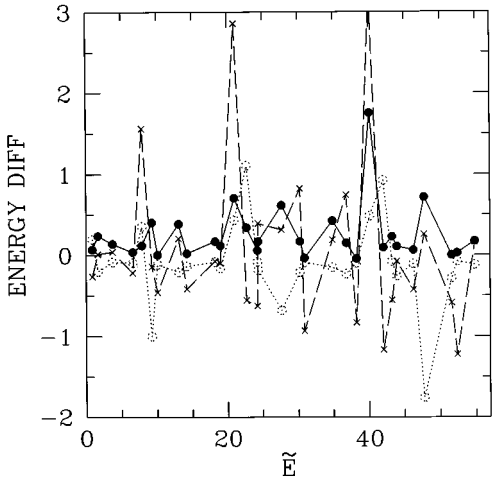


FIG. 13. Deviations of the scaled semiclassical energy eigenvalues from the exact scaled energy eigenvalues, $\widetilde{E}_{\rm ln}^{\rm sc}-E_{\rm ln}^{\rm exact}$, plotted against the scaled energy $\widetilde{E}$. Dotted circles joined by dotted lines: EBK approximation. Crosses joined by dashed lines: Bogomolny's approximation. Solid circles joined by solid lines: approximation including diffractive effects. System with $a=0.1R$.

for $E_{ln}$ which can be solved by an iterative procedure, starting from a good estimate for $E_{ln}$. The solution is the EBK energy eigenvalue. The scaled energy eigenvalues calculated in this way are given in column 3 of the tables.

At the bottom of column 3 is the rms deviation of the scaled EBK energy eigenvalues from the exact scaled energy eigenvalues. For the case $a=0.1R$, the rms deviation for the EBK eigenvalues is about half that obtained from Bogomolny's semiclassical approximation. However, for the other two cases, the rms deviation for the EBK eigenvalues is larger than the Bogomolny results. Thus the EBK quantization scheme appears to give good results when the radius of the inner circle of the annulus is small, but not very good results when it is larger. Roughly speaking, however, the EBK and Bogomolny semiclassical approximations are of comparable accuracy for the annulus billiard. In comparison to these, the results calculated with the inclusion of diffractive effects are significantly better.

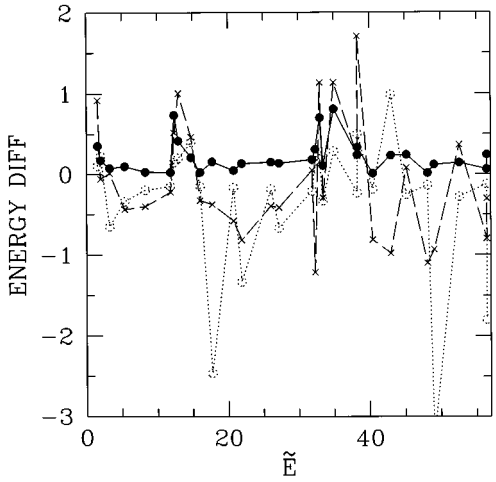


FIG. 14. The same as Fig. 13 for the system with $a=0.3R$.

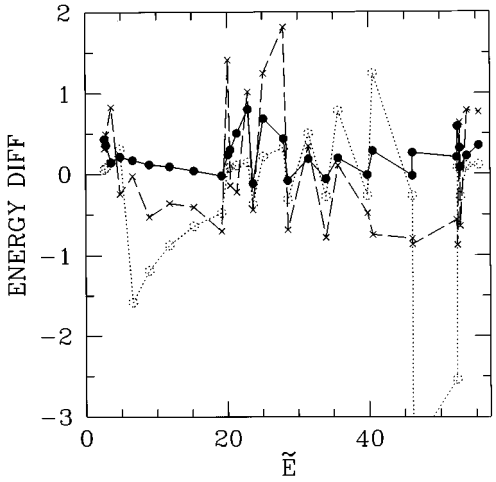


FIG. 15. The same as Fig. 13 for the system with $a=0.5R$.

Finally, the deviations of the semiclassical scaled energy eigenvalues from the exact scaled energy eigenvalues, $\widetilde{E}_{ln}^{\rm sc}-\widetilde{E}_{ln}^{\rm exact}$, are plotted against the scaled energy $\widetilde{E}$ in Figs. 13–15, for the first 30 distinct energy levels. The figures are for the three cases $a=0.1R$, $0.3R$, and $0.5R$, respectively. In each figure, the dotted circles (joined by dotted straight lines) show the deviations of the EBK eigenvalues, the crosses (joined by dashed lines) are the deviations of the Bogomolny eigenvalues, and the solid circles (joined by solid lines) are the deviations of the eigenvalues calculated with diffractive corrections. The plots show quite clearly that the deviations are smallest, on average, when diffractive corrections are included. Apart from that observation, which is consistent with the rms deviations given in the tables, the only pattern that we have found is that the three large positive peaks in Fig. 13, belonging to the Bogomolny approximation, correspond to the energy eigenvalues $(l=0,\ n=2)$, $(l=0,\ n=3)$, and $(l=0,\ n=4)$.

## VI. CONCLUSION

In this paper we have reported the results of a study of diffractive effects in a simple two-dimensional system, the annulus billiard. Starting from the boundary integral method, we obtained the exact quantum-mechanical transfer operator and two different semiclassical approximations of it. The simplest semiclassical approximation, formulated by Bogomolny [28], is constructed from purely classical (Newtonian) trajectories. To go beyond this, one must include the wave character of the quantum particle in some approximate way. Our studies of the annulus billiard, together with those of Primack *et al.* [27] on the Sinai billiard, show that the most important diffractive effects associated with a disk come from paths which lie in the penumbra, the region situated on both sides of the geometrical shadow boundary. By employing an expansion of the Green function appropriate for this region, we find that both the Green function and the transfer operator are brought into much better agreement with their exact quantum counterparts. Moreover, the corresponding semiclassical energy eigenvalues are much closer to the exact quantum energies, the rms deviation over the lowest 30

distinct eigenvalues being reduced by more than a factor of 2.

An advantage of the semiclassical approach is that, in contrast to the exact quantum-mechanical formulation, it enables one to interpret various features of the transfer operator. The large oscillations in the illuminated region in Figs. 7–9 have been identified as resulting from interference between the classical direct path and the path reflected from the inner circle (Fig. 10). Likewise, the steady decrease in $|T^{(p)}(\theta;k)|$ through the penumbra results from the Fresnel factor which almost completely turns off the direct contribution as $\theta$ goes from $\theta_{\rm ip}$ to $\theta_{\rm ps}$. In a representative case, we have found that the direct contribution (containing the Fresnel factor) and the glancing contribution are of comparable size near the shadow boundary (Fig. 11). Finally, when a shadow region exists as in Fig. 9, the contribution to the transfer operator in this region is barely visible on the plots.

As a last observation we note, from Eqs. (29)–(31) and Eq. (32), that the contributions to the transfer operator in the three regions are all of the same order in $\hbar$, namely, $\hbar^0$. However, if we consider the dependence on the wave vector $k$, it is evident that the contributions to the $T$ operator from the illuminated region and the direct term of Eq. (30) for the penumbra vary as $k^{1/2}$, whereas the contribution to Eq. (30) from the paths depicted in Fig. 2 and the shadow contribution based on Eq. (31) vary as $k^{1/3}$. Because of this small difference, the former contributions will become relatively more important as $k$ increases.

## ACKNOWLEDGMENTS

We would like to thank Niall Whelan for introducing us to diffractive effects in semiclassical physics, and for his help and encouragement. We would also like to thank Rajat Bhaduri, Julie Lefebvre, and Peiqing Tong for helpful suggestions at various stages of this project. This research was supported by the Natural Sciences and Engineering Research Council of Canada.

## APPENDIX: BOUNDARY POINTS BETWEEN THE REGIONS

In this appendix we describe how the boundary points of the three regions in Fig. 1 are determined. In what follows, the angle $\theta=\theta_j-\theta_0$ is taken to be less than $\pi$.

In the illuminated region, the Hankel functions $H_l^{\pm}(kR)$ and $H_l^{\pm}(ka)$ in Eq. (26) were approximated by the Debye asymptotic expansions [Ref. [38], Eq. (A.16)]. These expansions for $H_l^{\pm}(x)$ are valid for complex $l$ in the neighborhood of the positive real axis provided $0<\mathrm{Re}\{l\}<x$. The expansions fail for the reflected contribution to Eq. (29) when $|l-ka|\approx(ka)^{1/3}$, i.e., when $kR\cos(\theta/2)-ka\approx(ka)^{1/3}$. This sets the maximum permissible value of $\theta$ for the illuminated region at [27,39]

$$\theta_{i,\max}=2\cos^{-1}\left(\frac{ka+(ka)^{1/3}}{kR}\right). \tag{A1}$$

The condition for the validity of the approximations in the penumbra region, leading to Eq. (30), is [38,39]

$$|\cos^{-1}(a/R)-\theta/2|<(ka)^{-1/3}. \tag{A2}$$

Hence the penumbra region extends from $\theta_{p,\min}$ to $\theta_{p,\max}$, where

$$\theta_{p,\min}=2\cos^{-1}(a/R)-2(ka)^{-1/3}, \tag{A3}$$

$$\theta_{p,\max}=2\cos^{-1}(a/R)+2(ka)^{-1/3}. \tag{A4}$$

Calculations show that (when $ka>1$) $\theta_{i,\max}>\theta_{p,\min}$, implying that the illuminated region overlaps the penumbra. It is natural, therefore, to choose the boundary between the two regions to be $\theta_{\rm ip}=\frac{1}{2}(\theta_{i,\max}+\theta_{p,\min})$, which yields Eq. (27).

If Eq. (A4) yields a value for $\theta_{p,\max}$ greater than $\pi$, there is no shadow region. However, when a shadow region exists and the summation in Eq. (31) is performed over the first few zeros of $H_l^{+}(ka)$, the contribution from further zeros may be neglected provided [Ref. [38], Eq. (5.10)] $\gamma_0>(ka)^{-1/3}$, where $\gamma_0$ is the *creeping angle* similar to that shown in the lower part of Fig. 3. Since $\theta=2\cos^{-1}(a/R)+\gamma_0$, the *minimum* permissible value of $\theta$ in the shadow region is

$$\theta_{s,\min}=2\cos^{-1}(a/R)+(ka)^{-1/3}, \tag{A5}$$

which is less than $\theta_{p,\max}$. Therefore, the boundary between the penumbra and the shadow region will be taken to be $\theta_{\rm ps}=\frac{1}{2}(\theta_{p,\max}+\theta_{s,\min})$, which gives Eq. (28).

[1] M. C. Gutzwiller, J. Math. Phys. **12**, 343 (1971).
[2] M. C. Gutzwiller, *Chaos in Classical and Quantum Mechanics* (Springer-Verlag, New York, 1990).
[3] M. V. Berry, in *Quantum Chaos and Statistical Nuclear Physics*, edited by T. H. Seligman and H. Nishioka, Lecture Notes in Physics Vol. 263 (Springer, Berlin, 1986), p. 1.
[4] A. Voros, J. Phys. A **21**, 685 (1988).
[5] R. Artuso, E. Aurell, and P. Cvitanović, Nonlinearity **3**, 325 (1990); **3**, 361 (1990).
[6] M. Sieber and F. Steiner, Phys. Rev. Lett. **67**, 1941 (1991).
[7] M. V. Berry and J. P. Keating, Proc. R. Soc. London Ser. A **437**, 151 (1992).
[8] T. Szeredi and D. A. Goodings, Phys. Rev. E **48**, 3529 (1993).
[9] P. Gaspard and D. Alonso, Phys. Rev. A **47**, R3468 (1993).
[10] D. Alonso and P. Gaspard, CHAOS **3**, 601 (1993).
[11] G. Vattay and P. E. Rosenqvist, Phys. Rev. Lett. **76**, 335 (1996).
[12] B. R. Levy and J. B. Keller, Commun. Pure Appl. Math. **XII**, 159 (1959).
[13] J. B. Keller, J. Opt. Soc. Am. **52**, 116 (1962).
[14] A. Wirzba, CHAOS **2**, 77 (1992).
[15] A. Wirzba, Nucl. Phys. **A560**, 136 (1993).
[16] G. Vattay, A. Wirzba, and P. E. Rosenqvist, Phys. Rev. Lett. **73**, 2304 (1994).
[17] P. E. Rosenqvist, G. Vattay, and A. Wirzba, J. Stat. Phys. **83**, 243 (1996).

[18] N. Pavloff and C. Schmit, Phys. Rev. Lett. **75**, 61 (1995).
[19] N. D. Whelan, Phys. Rev. E **51**, 3778 (1995).
[20] N. D. Whelan, Phys. Rev. Lett. **76**, 2605 (1996).
[21] H. Bruus and N. D. Whelan, Nonlinearity **9**, 1023 (1996).
[22] P. Seba, Phys. Rev. Lett. **64**, 1855 (1990).
[23] P. Rosenqvist, N. D. Whelan, and A. Wirzba, J. Phys. A **29**, 5441 (1996).
[24] G. Date, S. R. Jain, and M. V. N. Murthy, Phys. Rev. E **51**, 198 (1995).
[25] M. Brack, R. K. Bhaduri, J. Law, C. Meier, and M. V. N. Murthy, CHAOS **5**, 317 (1995).
[26] S. M. Reimann, M. Brack, A. G. Magner, J. Blaschke, and M. V. N. Murthy, Phys. Rev. A **53**, 39 (1996).
[27] H. Primack, H. Schanz, U. Smilansky, and I. Ussishkin, Phys. Rev. Lett. **76**, 1615 (1996), and unpublished.
[28] E. B. Bogomolny, Nonlinearity **5**, 805 (1992).
[29] E. B. Bogomolny, CHAOS **2**, 5 (1992).
[30] T. Szeredi, J. H. Lefebvre, and D. A. Goodings, Nonlinearity **7**, 1463 (1994).
[31] M. R. Haggerty, Phys. Rev. E **52**, 389 (1995).
[32] M. V. Berry and M. Wilkinson, Proc. R. Soc. London Ser. A **392**, 15 (1984).
[33] P. A. Boasman, Ph.D. thesis, University of Bristol, 1992 (unpublished).
[34] P. A. Boasman, Nonlinearity **7**, 485 (1994).
[35] M. V. Berry and M. E. Mount, Rep. Prog. Phys. **35**, 315 (1972).
[36] J. H. Lefebvre, Ph.D. thesis, McMaster University, 1995.
[37] C. Rouvinez and U. Smilansky, J. Phys. A **28**, 77 (1995).
[38] H. M. Nussenzveig, Ann. Phys. **34**, 23 (1965).
[39] N. C. Snaith (unpublished). Copies of this work are available on request.
[40] M. Kac, Am. Math. Mon. **73**, 1 (1966).